Supporting Information for

Multimodal Nonlinear Optical Imaging of MoS_2 and MoS_2-Based van der Waals Heterostructures

Dawei Li,[†, ±] Wei Xiong,[†,§, ±] Lijia Jiang,[†] Zhiyong Xiao,[‡] Hossein Rabiee Golgir,[†] Mengmeng Wang,[†] Xi Huang,[†] Yunshen Zhou,[†] Zhe Lin,[†] Jingfeng Song,[‡] Stephen Ducharme,[‡] Lan Jiang,[≠] Jean-Francois Silvain,[#] and Yongfeng Lu[†,]*

[†] Department of Electrical and Computer Engineering, University of Nebraska-Lincoln, Lincoln, NE 68588-0511, United States

[§] Wuhan National Laboratory for Optoelectronics, Huazhong University of Science and Technology, 1037 Luoyu Road, Wuhan 430074, China

[‡] Department of Physics and Astronomy, Nebraska Center for Materials and Nanoscience, University of Nebraska-Lincoln, Lincoln, NE 68588-0511, United States

[≠] School of Mechanical Engineering, Beijing Institute of Technology, Beijing, 100081, China

[#] Institut de Chimie de la Matière Condensée de Bordeaux, Avenue du Docteur Albert Schweitzer F-33608 Pessac Cedex, France

[±] D.W. Li and W. Xiong contributed equally to this work.

* Address correspondence to: ylu2@unl.edu

Contents:

S1. The Schematic of Multiphoton Nonlinear Optical Microscopic System ….. 3

S2. Spectra of Pump and Probe Laser Beams.....4

S3. Nonlinear Optical Spectral Analyses of Trilayer MoS_2 6

S4. Polarization-Resolved Multiphoton Nonlinear Optical Characterization 8

S5. Determination of Crystal Orientation of MoS_2 Atomic Layers.....11

S6. Nonlinear Optical Spectrum and Imaging of Monolayer $MoSe_2$ 14

S7. Characterization of a Few-Layer MoS_2 Sample with Different Thicknesses.....15

S8. Nonlinear Optical Imaging of a Thick MoS_2 Flake.....16

S9. Comparison of SFG and SHG in Odd-Layered MoS_2.....17

S10. Growth of MoS_2 Thin Films 18

S11. Raman and PL Characterizations of MoS_2 Thin Films Grown by the SSS Method 19

S12. Nonlinear Optical Imaging of MoS_2 Thin Films Grown by the SSS Method.....21

S13. Thickness measurement of A SSS-Grown MoS_2 Thin Film by AFM 22

S14. Nonlinear Optical Mapping of Thermal Oxidation Process in a Few-Layer MoS_2 Sample.....23

S15. Nonlinear PL spectra of a Few-Layer Graphene Induced by Fs Laser Irradiation 24

S16. Nonlinear Optical Imaging of MoS_2-Graphene Heterostructures 25

S17. Raman/PL Spectra of MoS_2-Graphene Heterostructure.....26

S18. Influence of Interlayer Spacing in the MoS_2-Graphene Heterostructures on the Nonlinear Optical Properties 27

References.....28

S1. The Schematic of Multiphoton Nonlinear Optical Microscopic System

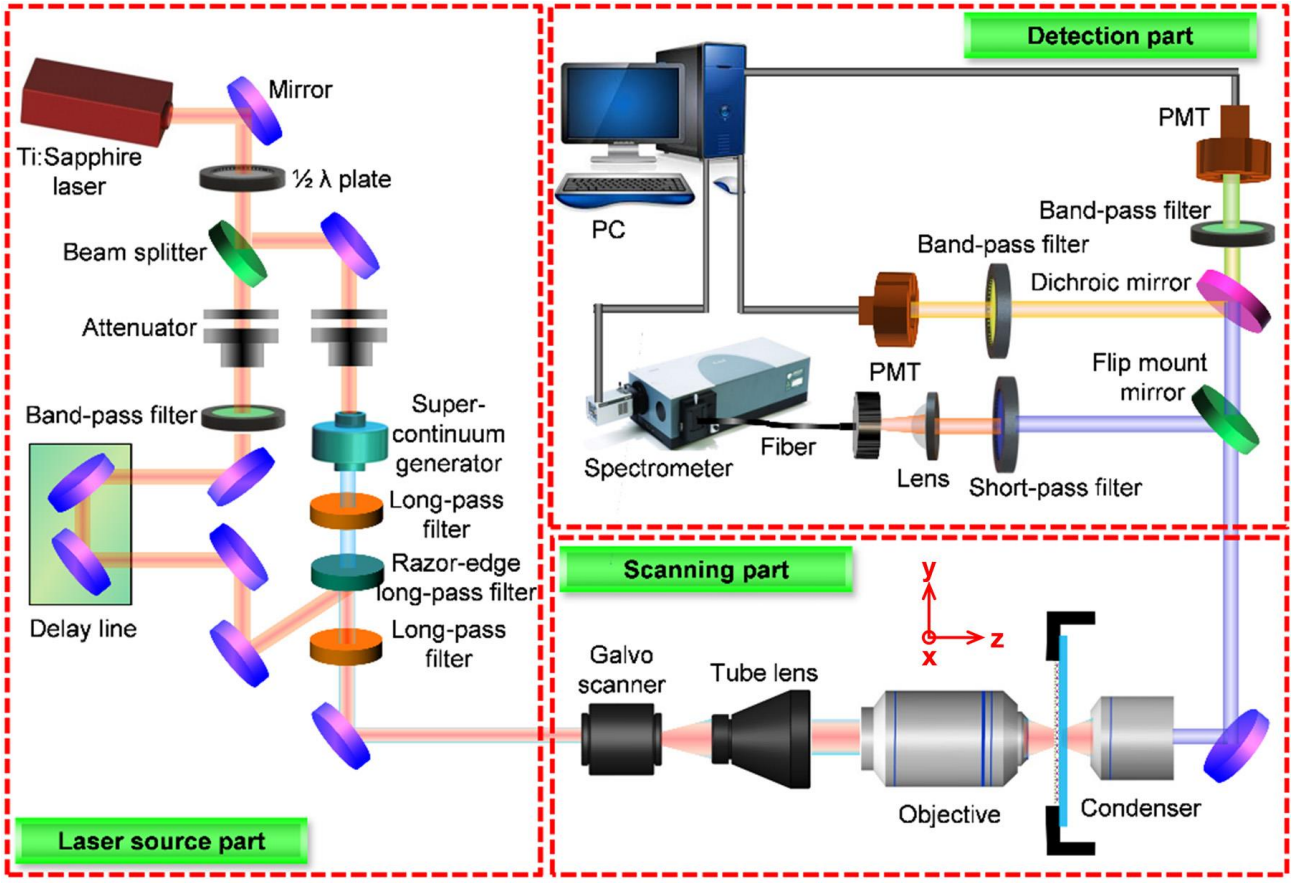

Figure S1. The schematic setup of multiphoton nonlinear optical microscopic system. Two incident laser beams with wavelengths λ_{pump} (tunable from 780 to 820 nm) and λ_{probe} (820 to 1100 nm) are used to optically excite MoS_2 and MoS_2-based heterostructure samples.

S2. Spectra of Pump and Probe Laser Beams

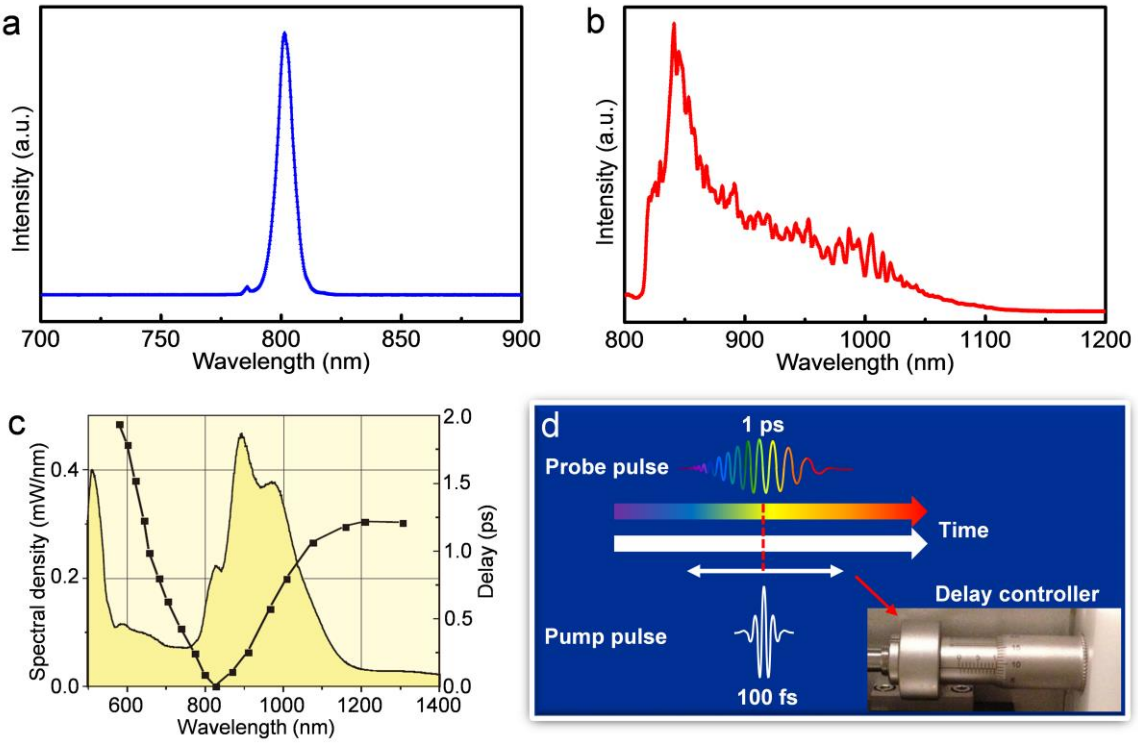

Figure S2. Spectra of two incident laser beams. (a) Pump and (b) probe laser beams. (c) The group delay for different spectral components of photonic crystal fiber (PCF) pumped by an 800 nm fs laser and 150 mW power.[1] (d) Realization of multiphoton nonlinear optical response by tuning the temporal delay between the pump and probe beams.

Figures S2 (a,b) show the spectra of the (a) pump and (b) probe laser beams with wavelengths λ_{pump} (800 nm) and λ_{probe} (820 to 1100 nm), respectively. In our experiment, both the pump and probe beams were provided by a single femtosecond (fs) laser (MaiTai DeepSee HP, SpectraPhysics) in conjunction with a supercontinuum generator (SCG, Newport). The SCG is actually a photonic crystal fiber (PCF) 12 cm in length, which allows a board supercontinuum to be generated by coupling an ultrafast laser pulse.

According to the data note,[1] different spectral components are generated in different parts of the PCF; and additional time delays are acquired during the propagation through the fiber. The group delay between 820 and 1100 nm components of our broadband probe beam was ~ 1.0 ps (Figure S2c). The pump beam used in this work was 800 nm with a pulse duration of ~ 100 fs. Thus, we

tuned the temporal delay between the pump and the probe to realize the multiphoton nonlinear response (such as sum-frequency generation and four-wave mixing) with different pump-probe color pairs (Figure S2d).

S3. Nonlinear Optical Spectral Analyses of Trilayer MoS_2

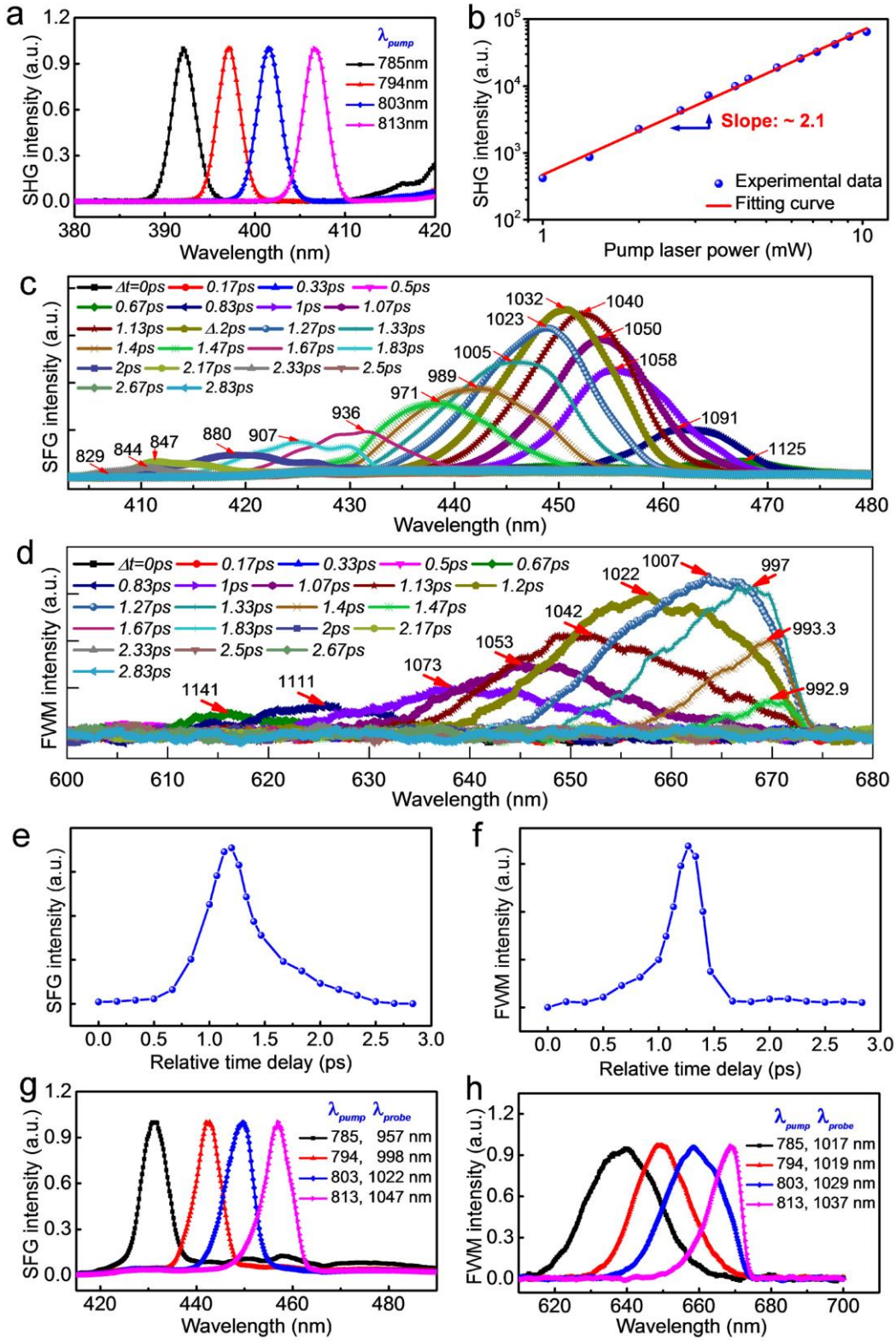

Figure S3. Normalized nonlinear optical spectra from a trilayer MoS_2 sample (shown in Figure 1) excited with different pump-probe wavelengths and delays. (a) SHG spectra at different pump wavelengths. (b) Pump laser power dependence of the SHG intensity. Time-

dependence of (c,e) SFG and (d,f) FWM responses excited with 800 nm pump and broad-band probe beams. (g) Pump-probe wavelength (λ_{pump}, λ_{probe}): (785, 983 nm), (794, 998 nm), (803, 1015 nm), (813, 1027 nm) dependence of the SFG spectra. (h) Pump-probe wavelength (λ_{pump}, λ_{probe}): (785, 1017 nm), (794, 1013 nm), (703, 1029 nm), (813, 1037 nm) dependence of the FWM spectra.

S4. Polarization-Resolved Multiphoton Nonlinear Optical Characterization

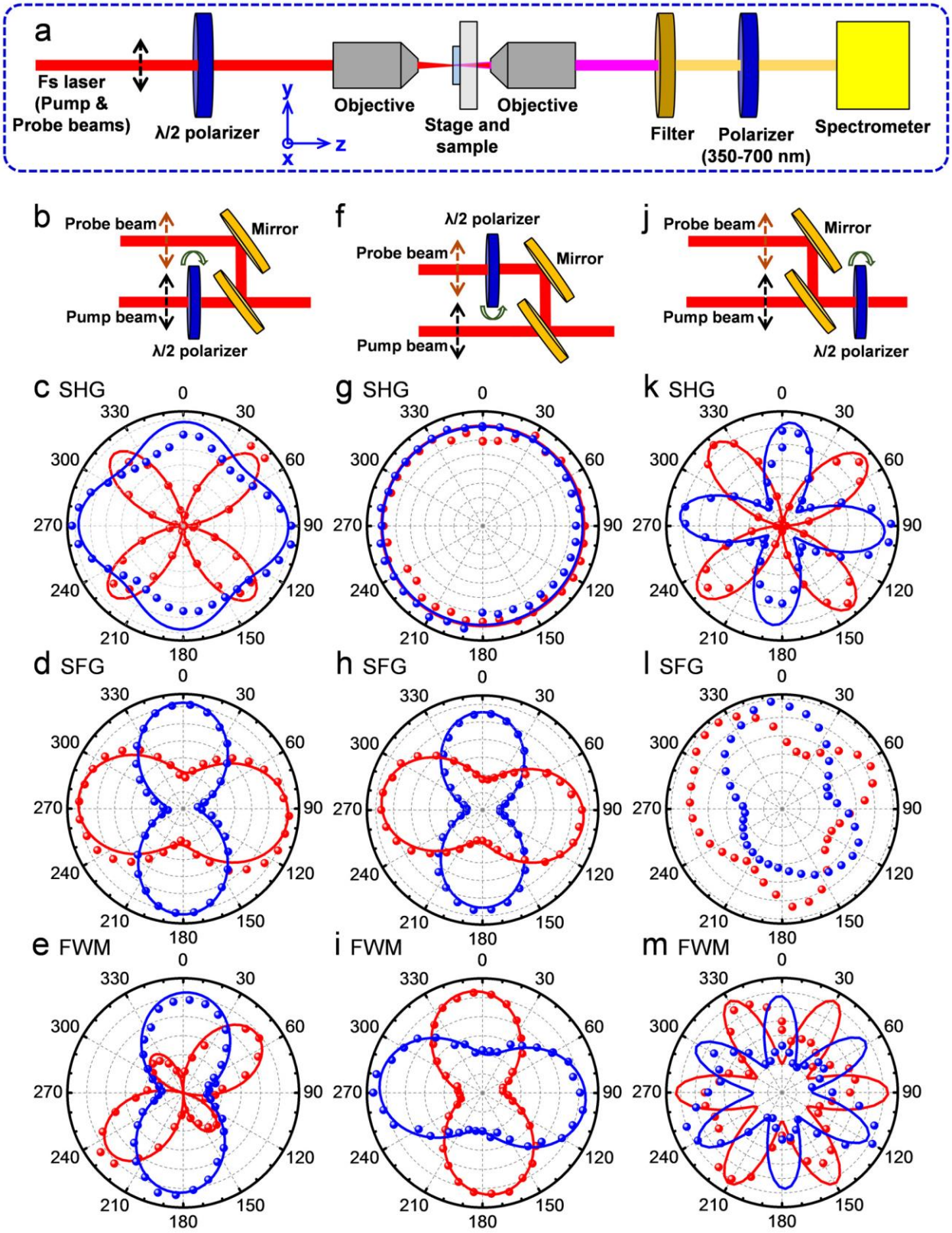

Figure S4. The polar plots of nonlinear optical signals in *y*-polarization (blue) and *x*-polarization (red) generated as functions of the incident polarization angle for a MoS_2 crystal shown in Figure 1. (a) Optical layouts for polarized SHG, SFG, and FWM measurements. (b-e)

Pump beam rotating with fixed probe beam. (f-i) Probe beam rotating with fixed pump beam. (j-m) Both beams rotate simultaneously. (c,g,k) SHG, (d,h,l) SFG, and (e,i,m) FWM plots.

The polarization dependence of nonlinear optical signals were exploited to obtain more information about the orders of optical nonlinearity and the structure of the MoS_2 samples. Here, the dependence of nonlinear optical intensity (SHG, SFG, FWM) on the polarization of incident beam was investigated (Figure S4). The blue and red curves correspond to the polarized nonlinear optical signals perpendicular and parallel to the optical table (Figure S1), respectively. It can be clearly seen that different nonlinear optical modes show different periodic variation features. The polarization dependence of the SHG intensity is only determined by the pump beam (Figure S4c,g,k), while those of SFG and FWM are determined by both pump and probe beams (Figure S4d,h for SFG and Figure S4e,i for FWM), which is consistent with the observation as shown in Figure 1. In the case of SHG polarization dependence, a response with symmetrical four-lobe shape appears for I_{SHG}^{x} and I_{SHG}^{y}, where I_{SHG}^{x} and I_{SHG}^{y} can be well fitted using $A+I_{SHG}^{\max}\sin^2(2\theta+\theta_0)$ and $A+I_{SHG}^{\max}\cos^2(2\theta+\theta_0)$, respectively. The observed symmetry is consistent with the D_{3h} symmetry group for the odd-layered MoS_2. In the case of the SFG and FWM polarizations where only pump beam rotates (Figure S4d,e), dumb-bell and asymmetric four-lobe shape responses were observed for I_{SFG}^{x} and I_{FWM}^{x}; while in the case where only probe beam rotates, both polarized SFG and FWM intensities show a dumb-bell shape response (Figure S4h,i), further confirming $I_{SFG}\propto I_{pump}\cdot I_{probe}$ (second-order nonlinearity) and $I_{FWM}\propto I_{pump}^{2}\cdot I_{probe}$ (third-order nonlinearity). Compared with only pump (or probe) beam rotating, the case is different and complex for the polarization dependence of SFG and FWM intensities with simultaneous rotation of the pump and probe beams. The perpendicular and parallel polarizations of SFG intensities show irregular dumb-bell and three-ring shapes, respectively, with simultaneous rotation of the pump and probe beams (Figure S4l). However, we cannot find a suitable fitting function for the relationship between the polarization

resolved SFG and the polarization of the incident pump-probe beams. Interestingly, both perpendicular and parallel polarization components of the FWM intensities show a 60^{o} variation period as functions of the incident beam polarization, which can be fitted based on a six-fold pattern (Figure S4m), similar to that of SHG intensity as a function of the sample rotation angle, implying that the polarization dependence of the FWM can be used to identify crystal orientations of MoS_2 sheets. Though the source of the poor fitting in Figures S4l and S4m is still unclear, there are several possible reasons: 1) the broadband probe beam used in this work which may have influenced the pump-probe combinations and the nonlinear optical signals generated, and 2) background noise that originated from the weak emission signals generated by the broadband probe beam. From the results shown above, the rotation of the sample maybe no longer necessary for distinguishing crystalline orientations, which can be performed through SHG or FWM by rotating the polarization angle of the incident beams.

S5. Determination of Crystal Orientation of MoS_2 Atomic Layers

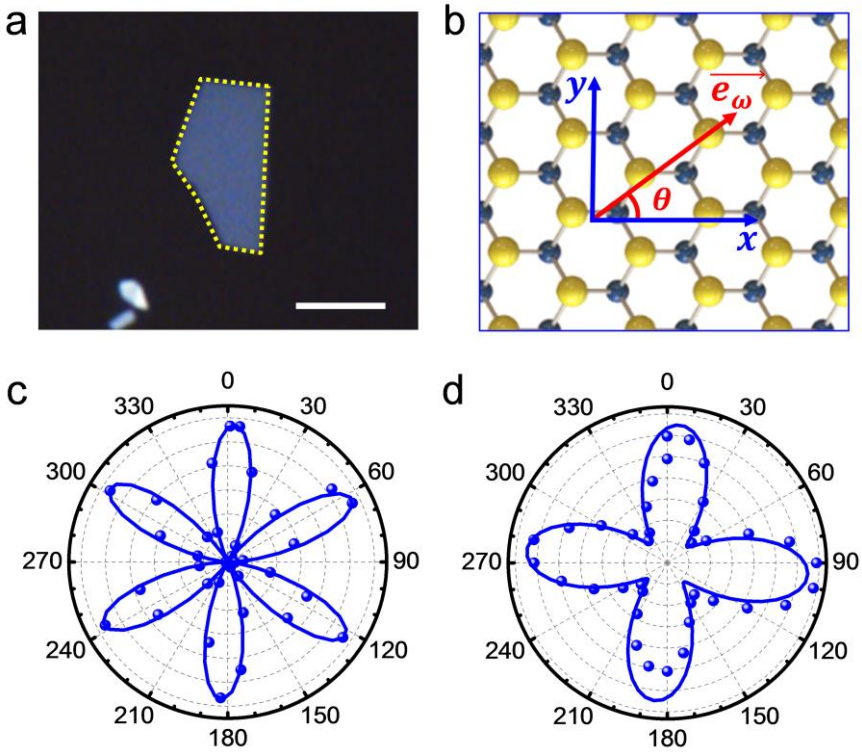

Figure S5. Comparison of different approaches for determination of crystal orientation of MoS_2 atomic layers based on SHG polarization analyses. (a) Optical image of a MoS_2 crystal shown in Figure 1. Scale bar: 10 μm. (b) The schematic of the MoS_2 crystal structure. (c,d) The polar plot of the parallel polarization SHG intensity as a function of (c) the sample rotation angle and (d) the incident pump polarization angle.

Different approaches can be used to determine the crystal orientations of MoS_2 atomic layers based on SHG polarization analyses. Here, we compared two approaches. The first is to rotate the MoS_2 sample and collect the SHG signal along the same polarization as the incident pump beam (Figure S5c).[2, 3] The second is to rotate the polarization of the incident pump beam and keep a fixed angle between the sample crystal orientation and the polarization of the SHG generated (Figure S5d).[4]

As we know, monolayer or odd-layered MoS_2 belongs to the D_{3h} point-group, which has only one independent $\chi^{(2)}$ component in the second-order nonlinear optical susceptibility tensor:

$\chi^{(2)} = \chi^{(2)}_{xxy} = \chi^{(2)}_{xyx} = \chi^{(2)}_{yxx} = -\chi^{(2)}_{yyy}$.[5] The SHG intensity generated can be defined as:

$$I_{2\omega} = \left|\overrightarrow{E_{2\omega}}\right|^2 \propto \left|\overrightarrow{e_{2\omega}} \cdot (\chi^{(2)}_{ijk} \cdot \overrightarrow{e_{\omega}}) \cdot \overrightarrow{e_{\omega}}\right|^2, \text{[3, 6]} \quad (1)$$

where $\overrightarrow{e_{\omega}}$ and $\overrightarrow{e_{2\omega}}$ are the polarization vectors for the beams at incident laser frequency and SHG frequency. Thus, using Eq. (1), the dependence of the SHG intensity generated as a function of the sample rotation angle for incident pump polarization ($\overrightarrow{e_{\omega}}$) parallel (or perpendicular) to the analyzer ($\overrightarrow{e_{2\omega}}$) can be obtained and expressed as $I_{\parallel}^{2\omega} \propto \cos^2(3\theta + \theta_0)$ (or $I_{\perp}^{2\omega} \propto \sin^2(3\theta + \theta_0)$), where θ is the angle between the incident pump polarization and the *x*-direction, and θ_0 is the initial crystal orientation of the MoS_2 sample. The polarization resolved SHG signal shows a strong dependence on crystal orientation (six-fold symmetry) (Figure S5c). Therefore, the crystal orientation of MoS_2 can be directly determined by rotating the sample and keeping a fixed angle between the polarizations of the incident pump beam and the SHG generated.

The crystal orientations of MoS_2 can also be determined by measuring the dependence of polarized SHG intensity as a function of the incident pump polarization angle.[4] Using Eq. (1), the polarization of the SHG electric field ($\overrightarrow{E_{2\omega}}$) along the *x*- and *y*-directions can be given by $E_x^{2\omega} \propto \cos(2\theta + \theta_0)$ and $E_y^{2\omega} \propto \sin(2\theta + \theta_0)$, where θ is the angle between the incident pump polarization and the *x*-direction, and θ_0 is a rotation of the MoS_2 crystal axes with respect to the *x*-direction. The dependence of polarized SHG intensity as a function of incident pump polarization can then be given by $I_x^{2\omega} \propto \left|E_x^{2\omega}\right|^2 \propto \cos^2(2\theta + \theta_0)$ and $I_y^{2\omega} \propto \left|E_y^{2\omega}\right|^2 \propto \sin^2(2\theta + \theta_0)$, showing a four-fold symmetry (Figure S5d). In addition, we can obtain $E_{2\omega} = E_x^{2\omega} \sin\theta + E_y^{2\omega} \cos\theta \propto \sin(3\theta + \theta_0)$ with $\overrightarrow{E_{2\omega}} \parallel \overrightarrow{e_0}$, and then $I^{2\omega} \propto \left|E_{2\omega}\right|^2 \propto \sin^2(3\theta + \theta_0)$ which is consistent with the results obtained using the first method (by rotating the sample angle).

In summary, the above two approaches lead to the same results, both of which can be used to determine the crystal orientations of the MoS_2 atomic layers.

S6. Nonlinear Optical Spectra and Imaging of Monolayer $MoSe_2$

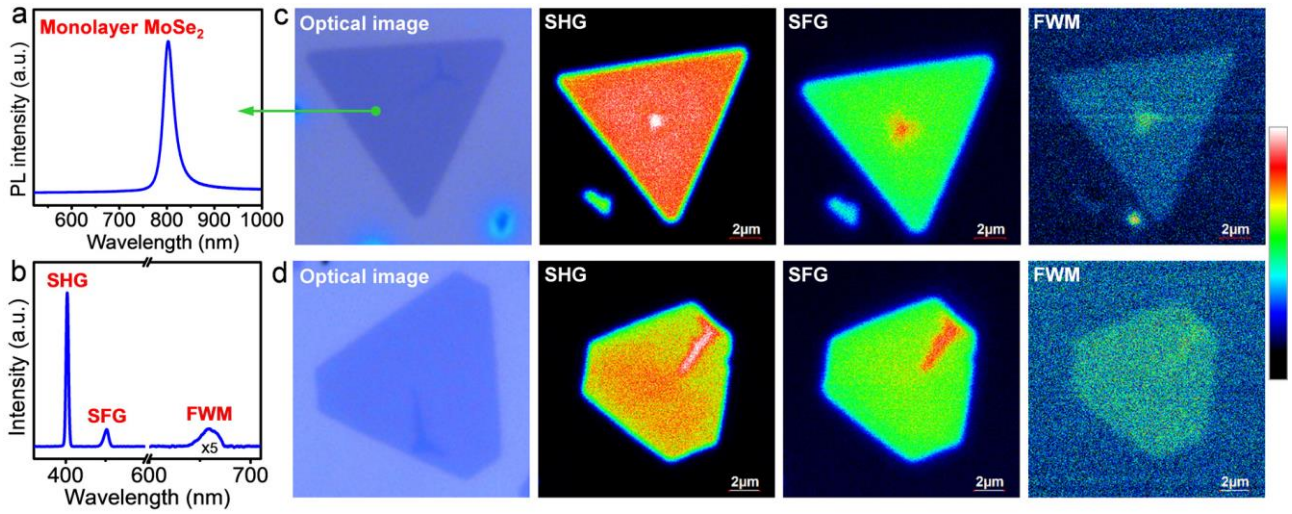

Figure S6. Nonlinear optical spectra and images of a $MoSe_2$ monolayer. (a) Photoluminesence (PL) and (b) nonlinear optical (SHG, SFG, FWM) spectra of a monolayer $MoSe_2$ shown in (c). (c, d) Optical and simultaneously detected SHG, SFG, FWM images of two monolayer $MoSe_2$ samples in different shapes: (c) regular triangle and (d) hexagon.

S7. Characterization of a Few-Layer MoS_2 Sample with Different Thicknesses

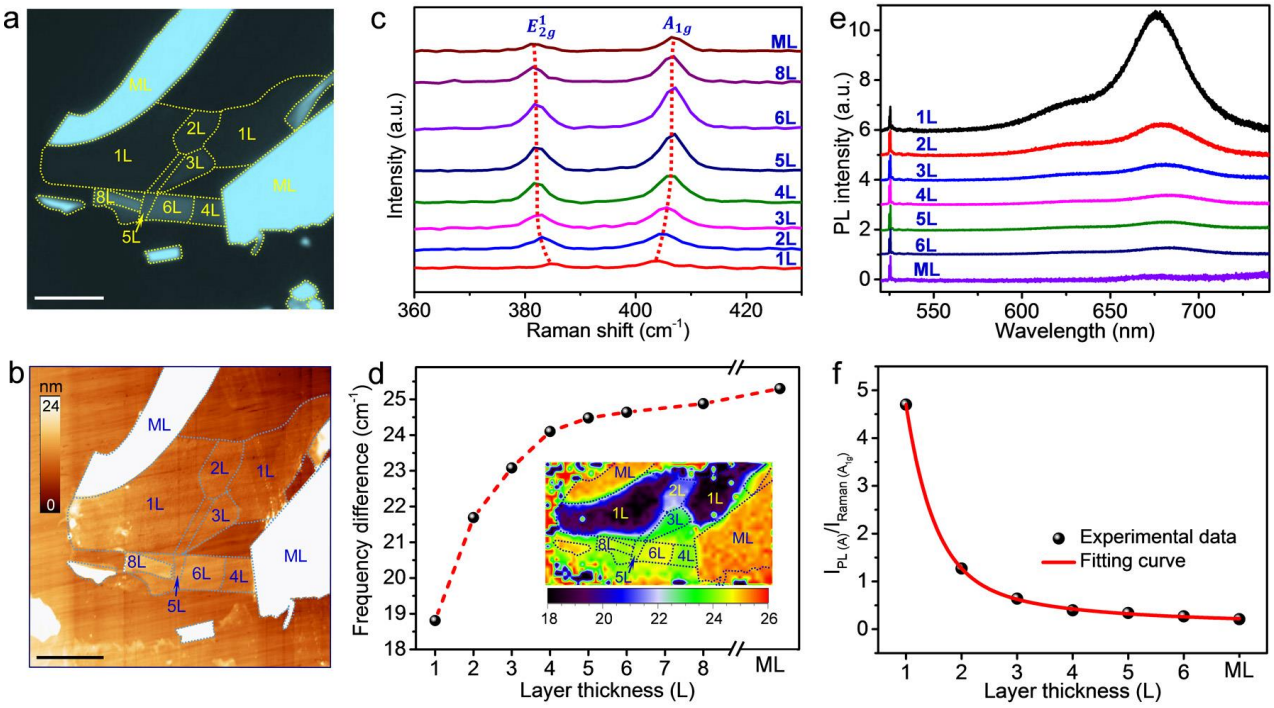

Figure S7. OM, AFM, Raman, and PL characterizations of a few-layer MoS_2 flake with different layer thicknesses, as show in Figure 2, in the main text. (a) OM and (b) AFM morphology. Scale bars: 5 μm. (c) Raman spectra of MoS_2 regions with differernt thicknesses. (d) Raman frequency difference (between E^1_{2g} and A_{1g}) as a function of the layer thickness. Inset in (d) shows the Raman mapping with frequency difference between A_{1g} and E^1_{2g}. (e) PL spectra normalized by Raman intensity of A_{1g} peak for the MoS_2 regions with different thicknesses. (f) Normalized PL peak intensity as a function of the MoS_2 layer thickness.

S8. Nonlinear Optical Imaging of a Thick MoS_2 Flake

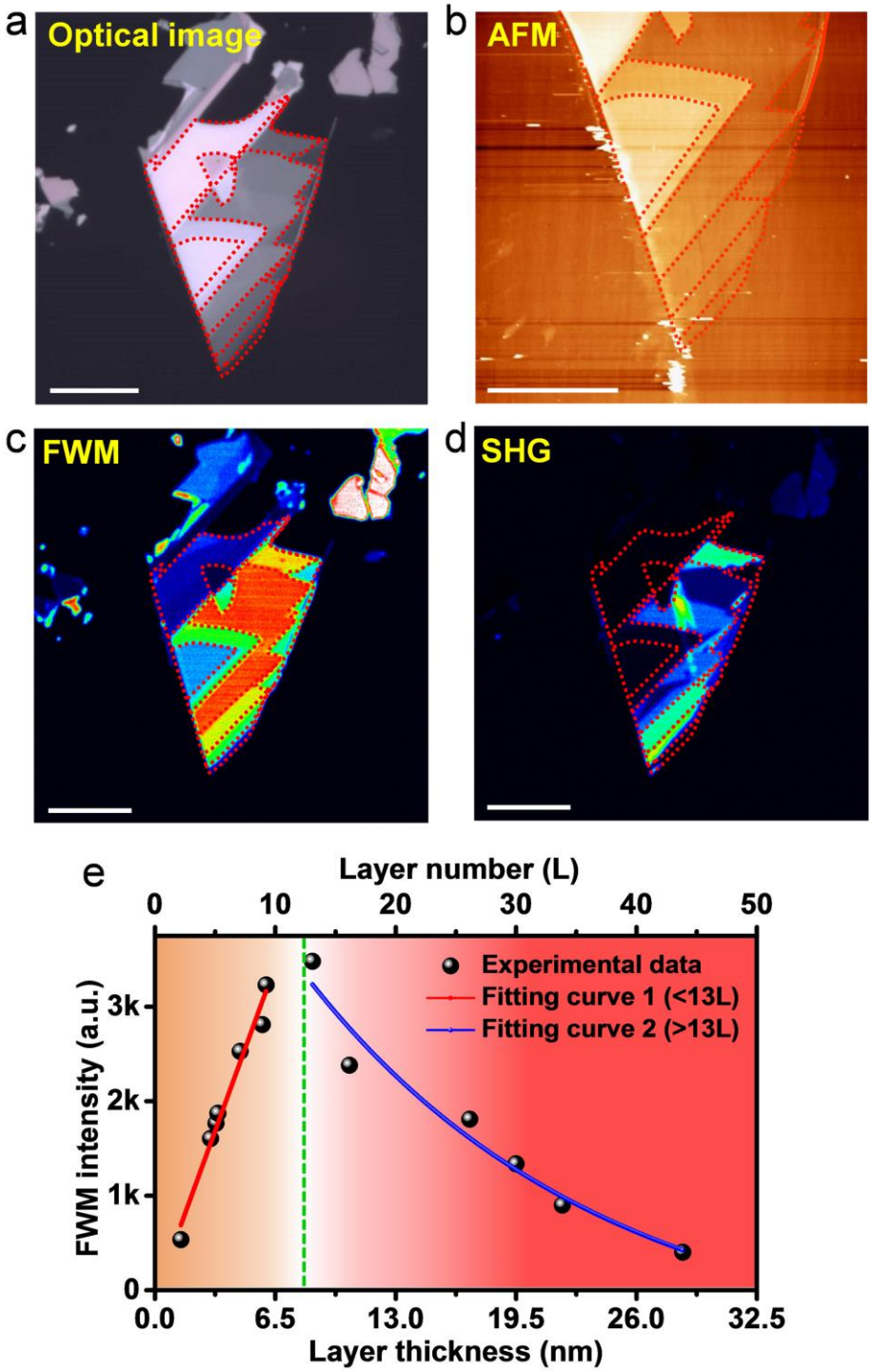

Figure S8. Nonlinear optical images of a thick MoS_2 flake with different thicknesses. (a) Optical micrograph, (b) AFM, (c) FWM, and (d) SHG images. Scale bars: 10 μm. (e) FWM intensity as a function of the MoS_2 layer thickness.

S9. Comparison of SFG and SHG in Odd-Layered MoS_2

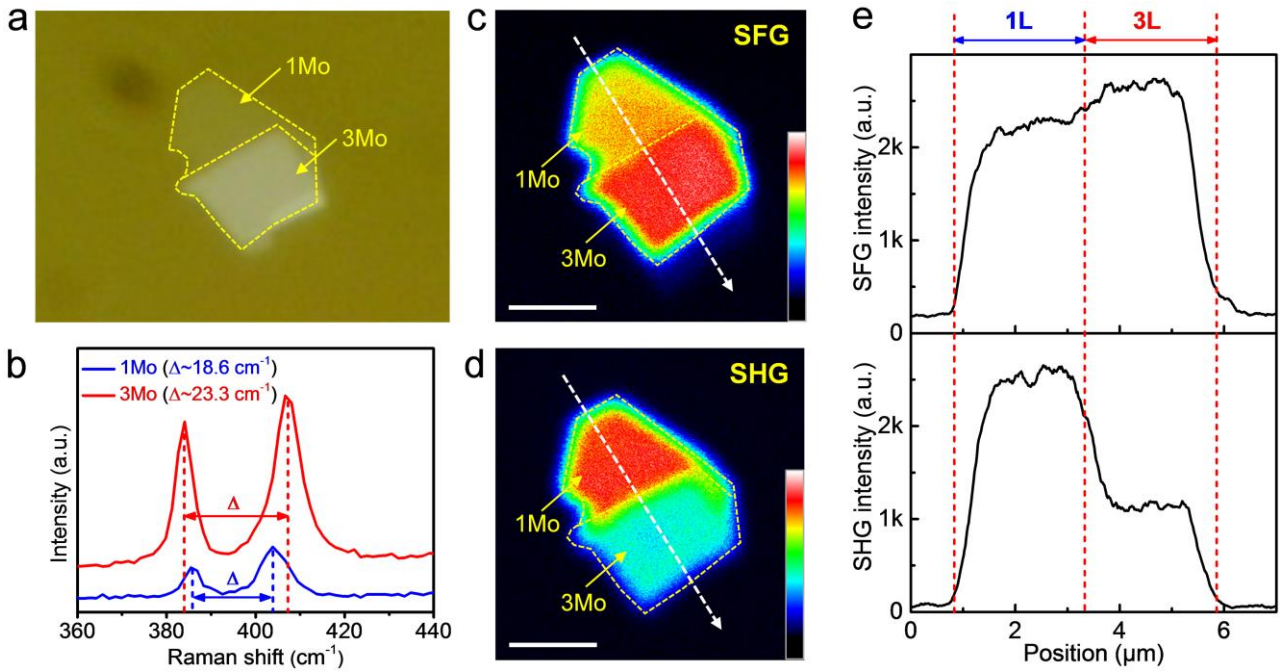

Figure S9. A typical mechanically exfoliated MoS_2 flake composed of a monolayer and a trilayer. (a) Optical image, (b) Raman spectra, (c) SFG, and (d) SHG. (e) Cross-sectional SFG and SHG intensity along the dashed lines shown in (c) and (d), respectively.

S10. Growth of MoS_2 Thin Films

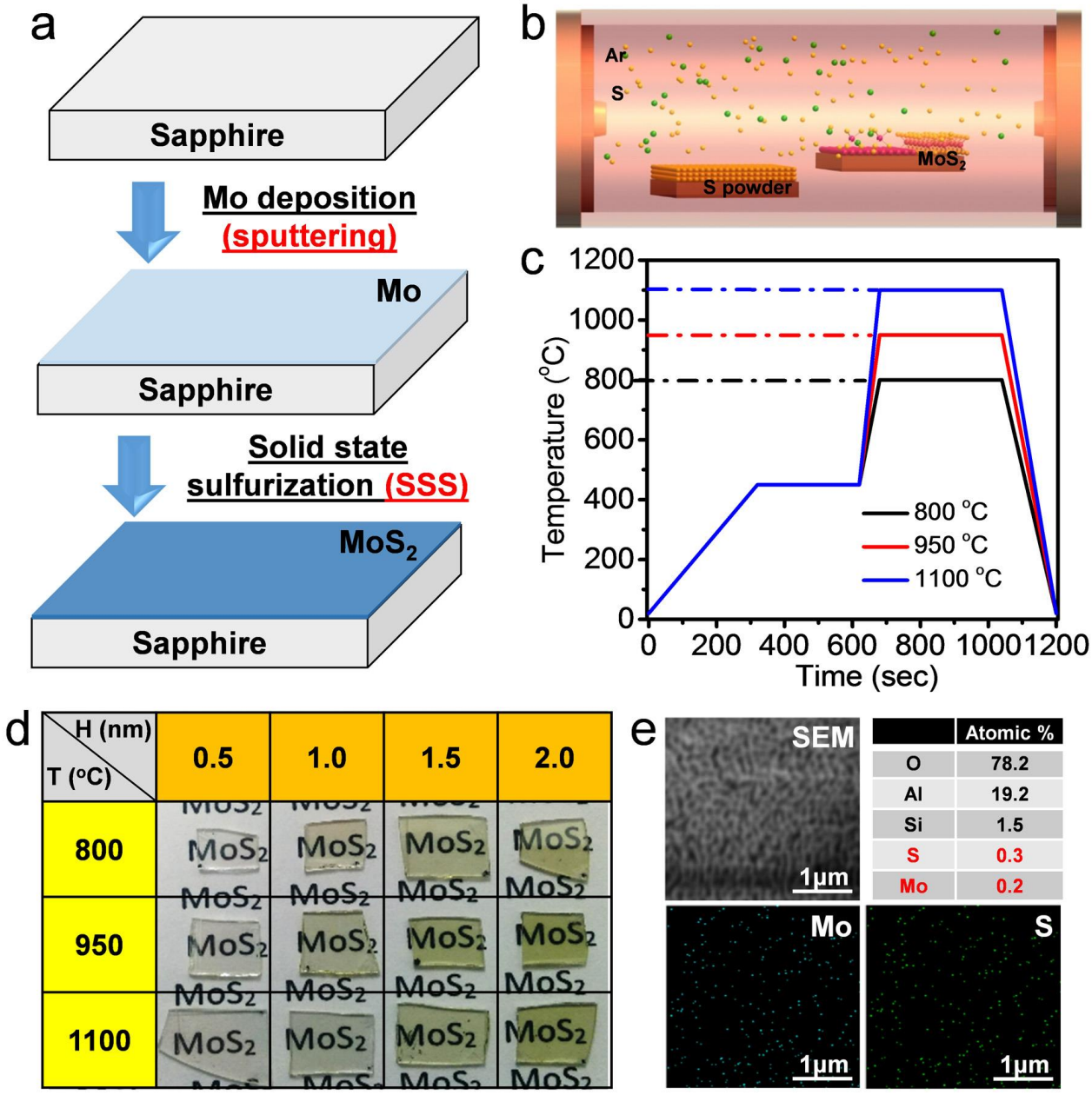

Figure S10. Growth of MoS_2 thin films using the solid state sulfurization (SSS) method. (a) The schematic of the MoS_2 growth process. Mo thin films with a thickness of several nanometers were deposited on a sapphire substrate by sputtering, which was then directly sulfurized to form MoS_2 thin films in a thermal furnace. (b) The schematic of the sulfurization process in the thermal furnace. (c) Temperature profile used in the growth of the MoS_2 thin films. (d) Optical photographs of the MoS_2 thin films deposited at different temperatures from Mo films of different thicknesses. (e) X-ray energy dispersive mapping analysis of MoS_2 thin films grown at 1100 °C from a Mo film with a thickness of ~ 1.5 nm.

S11. Raman and PL Characterization of MoS_2 Thin Films Grown by the SSS Method

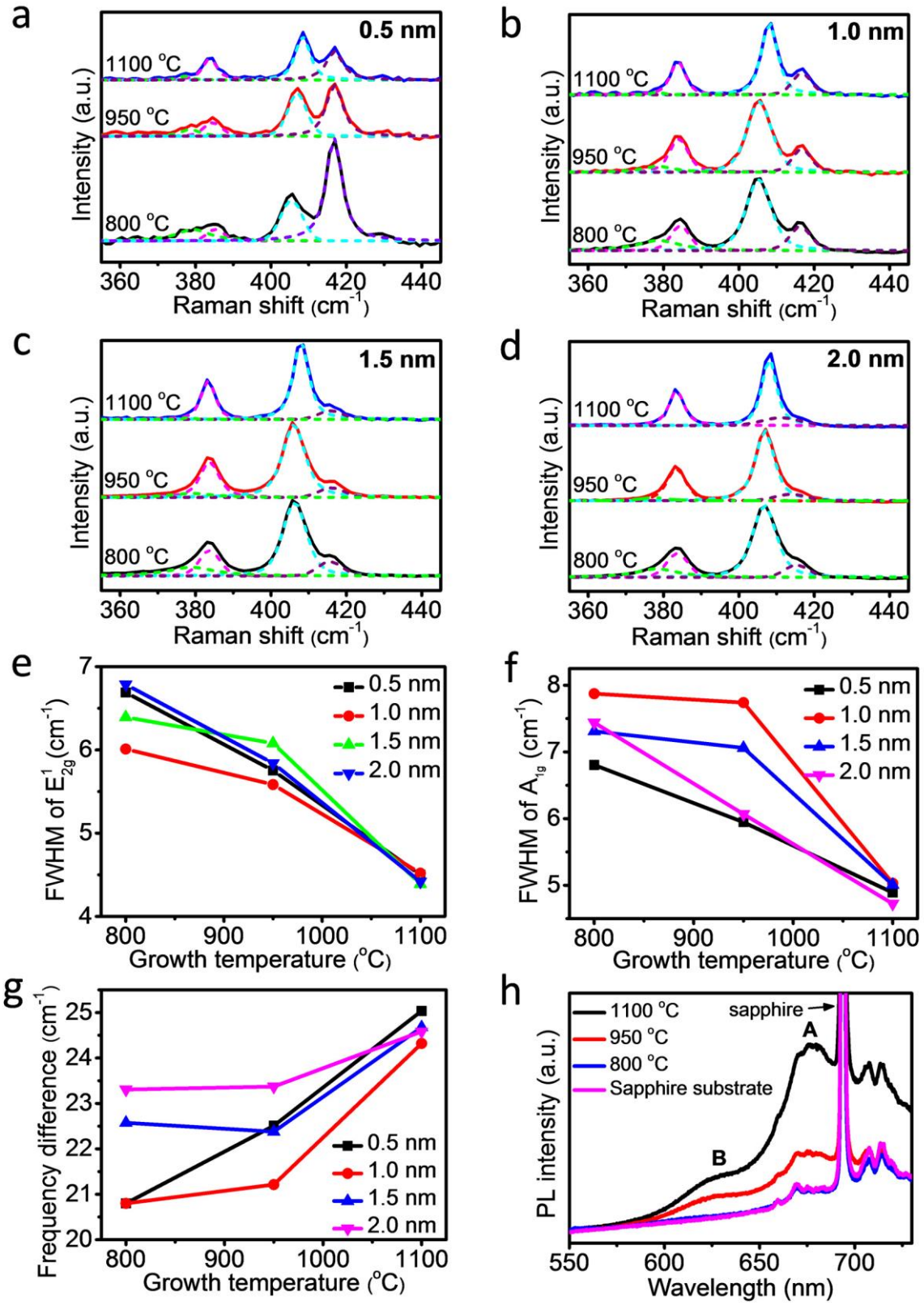

Figure S11. (a-d) Raman spectra from (a) 0.5, (b) 1, (c) 1.5, and (d) 2 nm thick Mo layers after sulfurization at different temperatures. (e-h) The full-width at half-maximum (FWHM) of (e) E^1_{2g}

and (f) A_{1g} peaks, and (g) frequency difference as functions of the growth temperature. (h) PL spectra from a 2 nm Mo layer after sulfurization at different growth temperatures.

Raman spectra of MoS_2 thin films grown at different temperatures from Mo films of different thicknesses are shown in Figure S11a-d. It is found from Figures S11e and f that FWHM of both E^1_{2g} and A_{1g} peaks are decreased with the increase in the growth temperature, which indicates that the structural quality of the MoS_2 grown significantly improves at a higher temperature. We also observed that the measured frequency difference between A_{1g} and E^1_{2g} increases as the growth temperature rises (Figure S11g). The frequency difference reaches the maximum value (near to the values of bulk MoS_2) at ~ 1100 ºC. However, the frequency difference cannot be used to determine whether or not the MoS_2 grown contains 2D crystalline structures of large grain sizes. The optical quality of the MoS_2 thin films grown was evaluated using PL spectroscopy, as shown in Figure S11h. No PL signal was observed at a low temperature (800 ºC), while two peaks can be found in the PL spectra as the growth temperature is above 950 ºC. This suggests an improved optical quality in the MoS_2 grown at higher temperatures.

S12. Nonlinear Optical Imaging of MoS_2 Thin Films Grown by the SSS Method

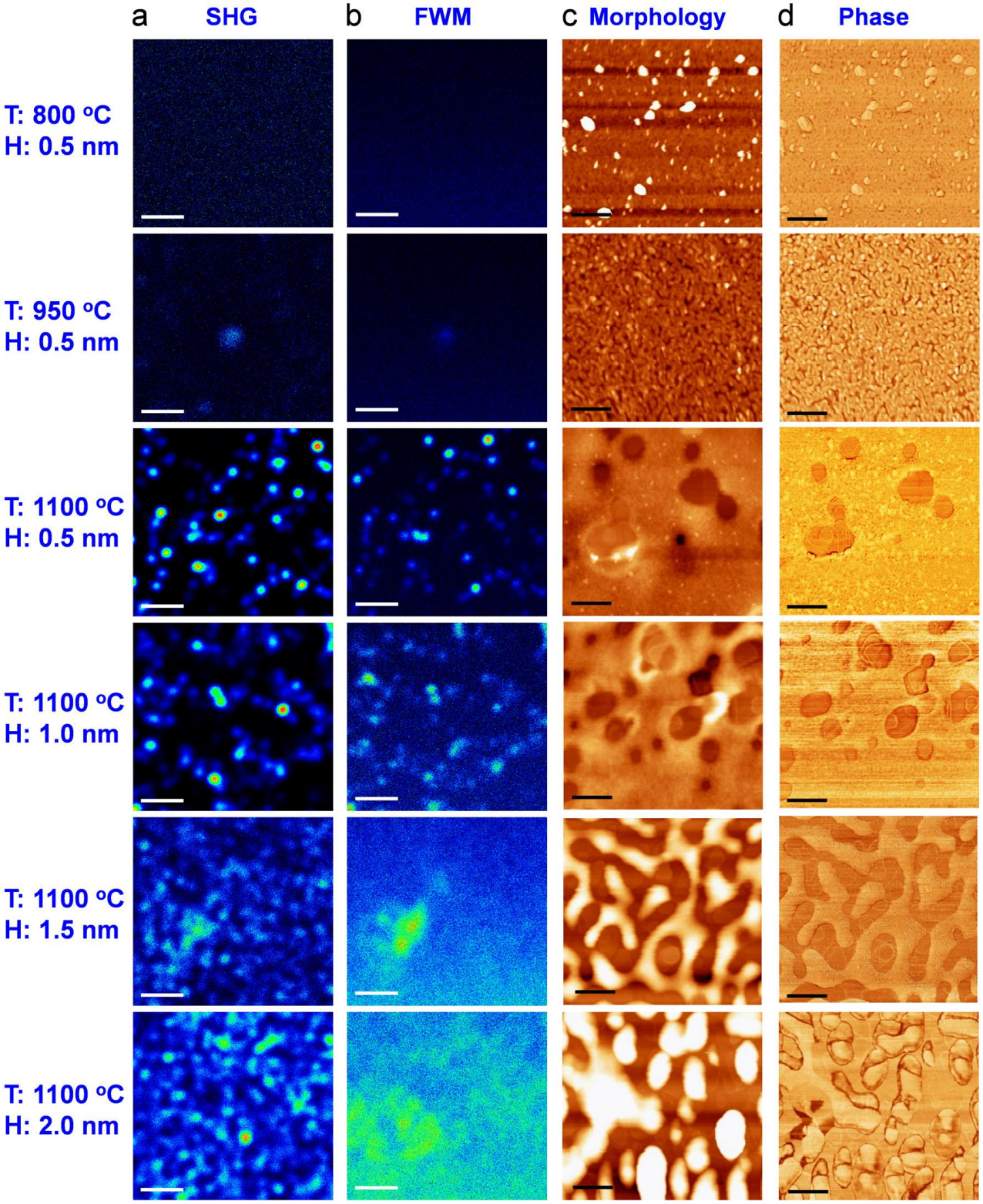

Figure S12. Characterizations of MoS_2 thin films on sapphire substrates grown at different temperatures from Mo films of different thicknesses. (a) SHG, (b) FWM, (c) AFM morphologies, and (d) AFM phases. Scale bars: 2 μm for (a,b) and 200 nm for (c,d).

S13. Thickness Measurement of a SSS-Grown MoS_2 Thin Film by AFM

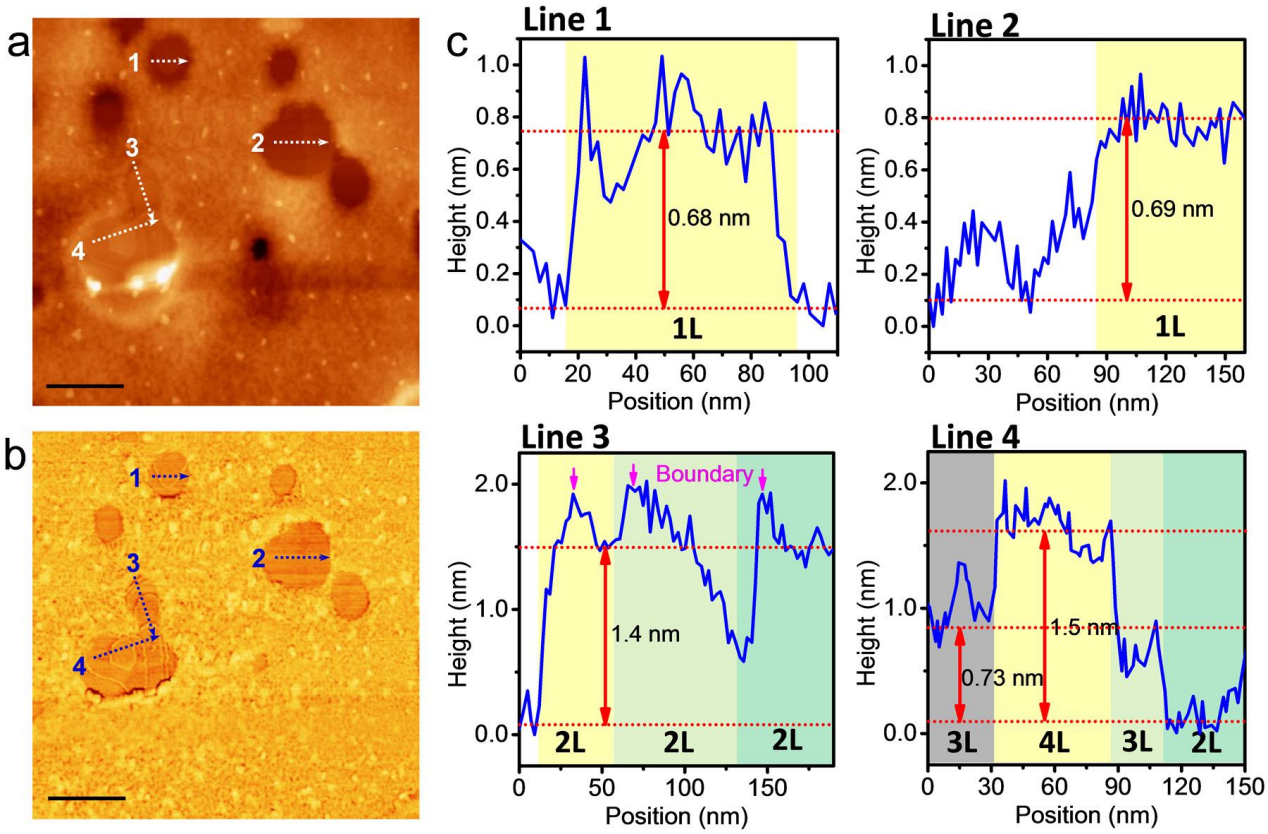

Figure S13. AFM images of a grown MoS_2 thin film, as show in Figure 3d, in the main text. (a) AFM height topography. (b) AFM phase. (c) Height profiles along the lines in (a). Scale bars: 200 nm.

S14. Nonlinear Optical Mapping of Thermal Oxidation Process in A Few-Layer MoS_2 Sample

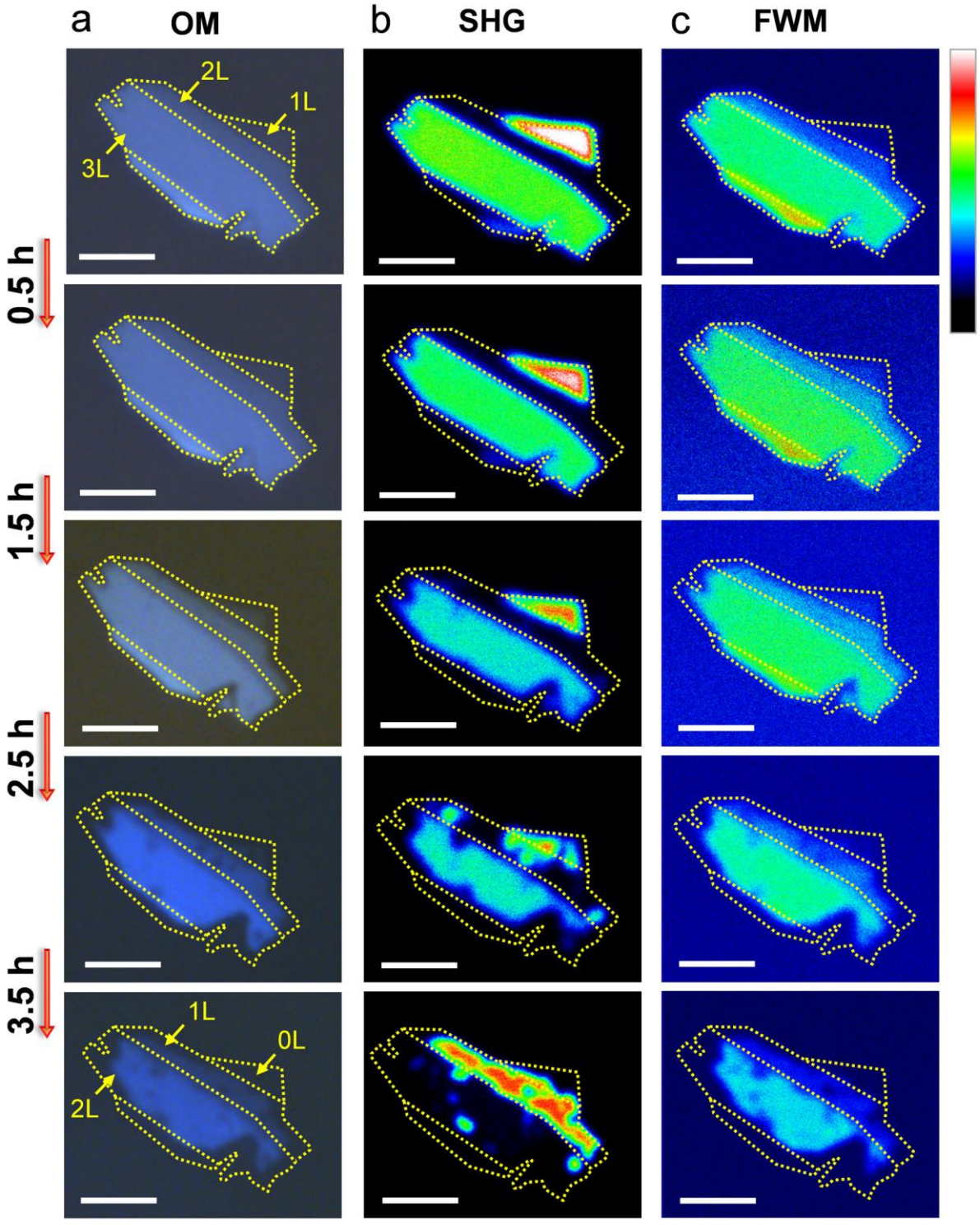

Figure S14. Thermal oxidation of a few-layer (1-3L) MoS_2 flake after different heating times. (a) OM, (b) SHG, and (c) FWM images acquired in between several heating/cooling steps. Scale bars: 3 μm.

S15. Nonlinear PL Spectra of a Few-Layer Graphene Induced by Fs Laser Irradiation[7]

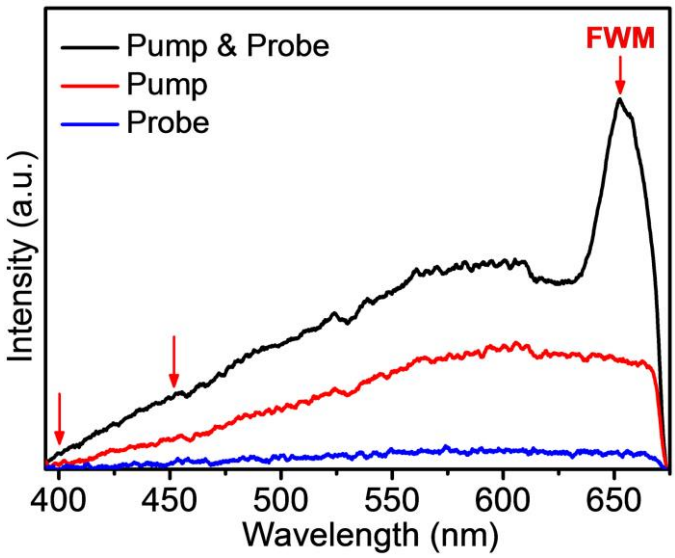

Figure S15. Nonlinear optical spectra from a few-layer graphene sample excited by pump-probe (black curve), pump (red curve), and probe (blue curve) laser beams. Sharp cuts at about 675 nm are due to the shortpass filter with a cut-off wavelength of 675 nm.

S16. Nonlinear Optical Imaging of MoS_2-Graphene Heterostructures

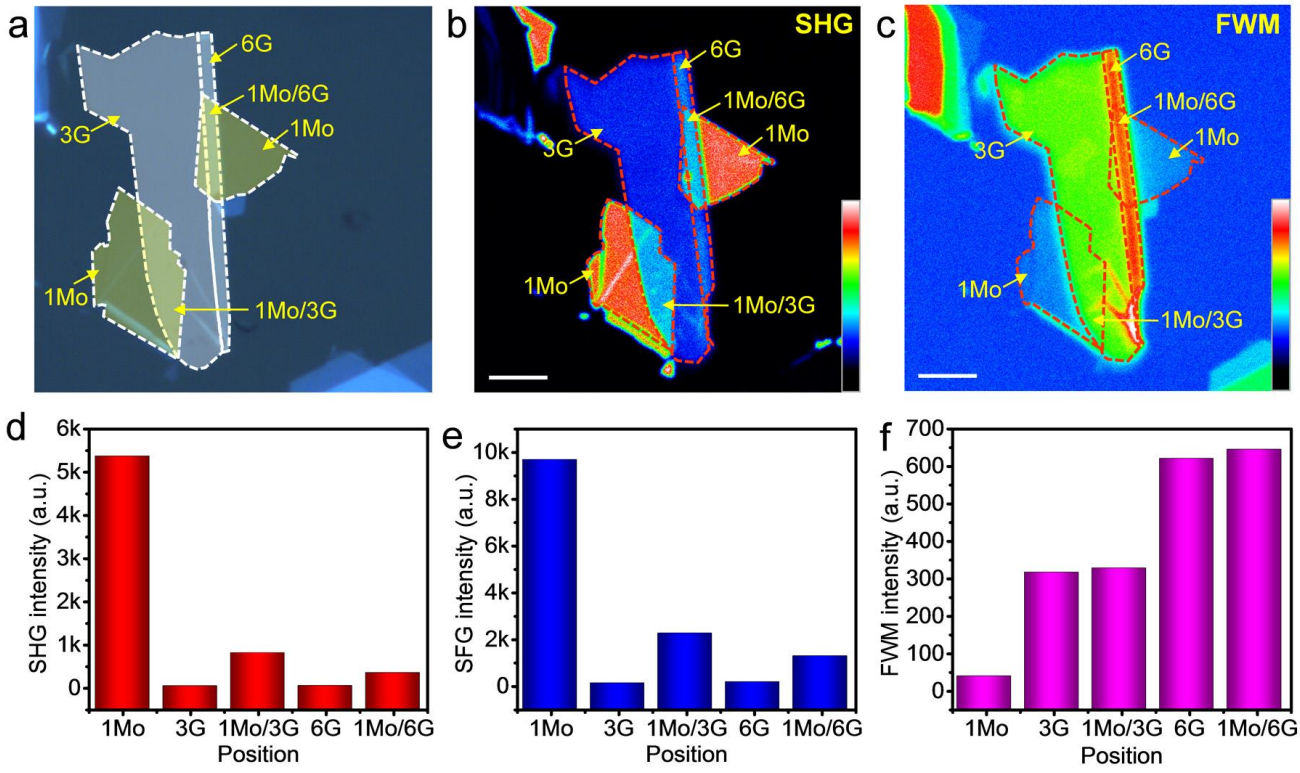

Figure S16. Nonlinear optical images of a MoS_2-graphene heterostructure [1L/(3L, 6L)]. (a) OM, (b) SHG, and (c) FWM images. Scale bars: 5 μm. (d-f) Nonlinear optical signal intensities of (d) SHG, (e) SFG, and (f) FWM from the MoS_2-graphene heterostructure in different regions.

S17. Raman/PL Spectra of MoS_2-Graphene Heterostructure

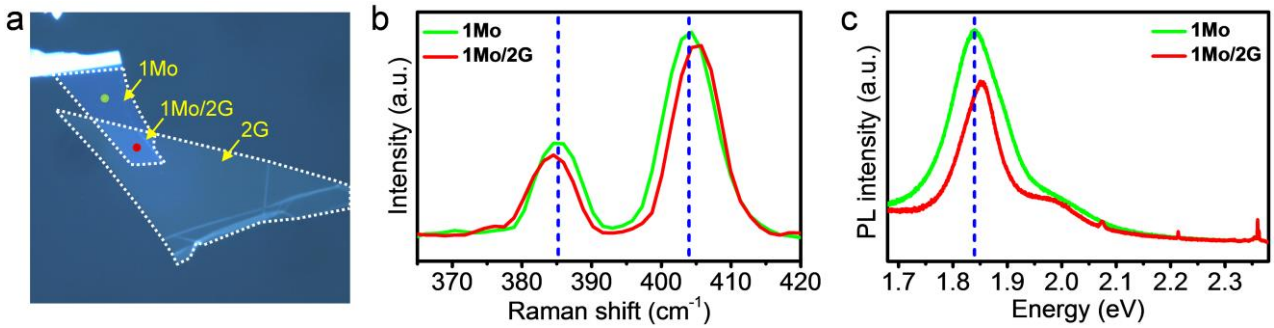

Figure S17. (a) Optical micrograph of the MoS_2-graphene heterostrcuture shown in Figure 5. (b) Raman and (c) PL spectra of MoS_2 in the regions as marked in (a).

S18. Influence of Interlayer Spacing in the MoS_2-Graphene Heterostructures on the Nonlinear Optical Properties

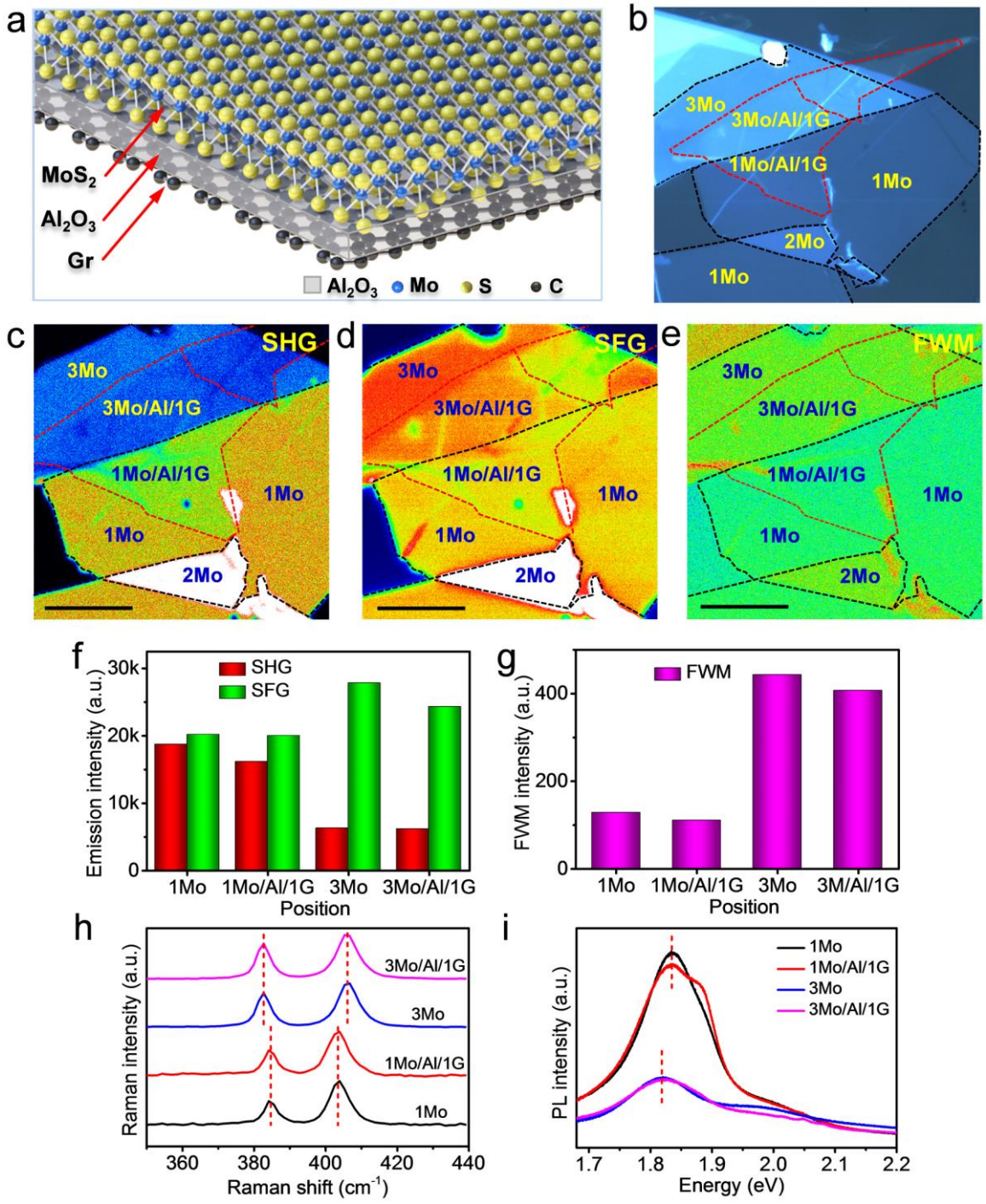

Figure S18. Characterizations of a MoS_2-graphene heterostructure with a ~ 1 nm Al_2O_3 film sandwiched in the heterostructure. (a) A schematic illustration of the MoS_2-Al_2O_3-graphene heterostructure. (b) OM, (c) SHG, (d) SFG, and (e) FWM images. Scale bars: 10 μm. Comparison of (f,g) nonlinear optical signal intensities, (h) Raman and (i) PL spectra of the MoS_2-Al_2O_3-graphene heterostructure in different regions.

REFERENCES

1. Newport Corporation Application Note. Supercontinuum Generation in SCG-800 Photonic Crystal Fiber. (Newport Corporation, 2006). http://www.newport.com/file_store/Optics_and_Mechanics/AppsNote28.pdf.
2. Zhang, X.-Q.; Lin, C.-H.; Tseng, Y.-W.; Huang, K.-H.; Lee, Y.-H. Synthesis of Lateral Heterostructures of Semiconducting Atomic Layers. *Nano Lett.* **2015**, *15*, 410-415.
3. Malard, L. M.; Alencar, T. V.; Barboza, A. P. M.; Mak, K. F.; de Paula, A. M. Observation of Intense Second Harmonic Generation From MoS_2 Atomic Crystals. *Phys. Rev. B* **2013**, *87*, 201401.
4. Mannebach, E. M.; Duerloo, K.-A. N.; Pellouchoud, L. A.; Sher, M.-J.; Nah, S.; Kuo, Y.-H.; Yu, Y.; Marshall, A. F.; Cao, L.; Reed, E. J.; Lindenberg, A. M. Ultrafast Electronic and Structural Response of Monolayer MoS2 under Intense Photoexcitation Conditions. *ACS Nano* **2014**, *8*, 10734-10742.
5. Boyd, R. W. *Nonlinear Optics, Third Edition*. Academic Press: 2008; p 640.
6. Yin, X.; Ye, Z.; Chenet, D. A.; Ye, Y.; O'Brien, K.; Hone, J. C.; Zhang, X. Edge Nonlinear Optics on a MoS_2 Atomic Monolayer. *Science* **2014**, *344*, 488-490.
7. Hendry, E.; Hale, P. J.; Moger, J.; Savchenko, A. K.; Mikhailov, S. A. Coherent Nonlinear Optical Response of Graphene. *Phys. Rev. Lett.* **2010**, *105*, 097401.